



Effect of heat treatment on mechanical properties of Ti–6Al–4V ELI alloy

B.D. Venkatesh, D.L. Chen*, S.D. Bhole

Department of Mechanical and Industrial Engineering, Ryerson University, 350 Victoria Street, Toronto, Ontario M5B 2K3, Canada

ARTICLE INFO

Article history:

Received 27 May 2008

Received in revised form

12 November 2008

Accepted 14 November 2008

Keywords:

Titanium alloy

Heat treatment

Mechanical properties

Strain hardening

Strain rate sensitivity

Fractal dimension

ABSTRACT

Ti–6Al–4V alloy of extra low interstitial (ELI) grade has been used in the biomedical applications because of its high strength-to-weight ratio and excellent biocompatibility. However, its relatively poor wear resistance leading to excessive wear and implant loosening requires proper surface hardening. The body implants are also subjected to a variety of loads at varying strain rates. The objective of this study was to evaluate the hardening behavior, strain rate sensitivity and fracture mechanisms with or without hardened surface layer. It was observed that the hardened surface layer had only a small effect on the strength but reduced the ductility. The yield strength (YS) and ultimate tensile strength (UTS) were higher in the water quenching and aging condition while the ductility was lower, when compared to the as-received condition and air cooling and aging condition. As the strain rate increased both YS and UTS increased and ductility decreased. The strain hardening exponent decreased with increasing strain rate. The strain rate sensitivity evaluated via both the common approach and Lindholm approach decreased as the true strain increased. Fractal dimension of fracture surfaces was observed to be associated with the heat treatment condition, ductility, fracture surface characteristics and roughness. The fractal dimension increased with increasing roughness of fracture surfaces.

© 2008 Elsevier B.V. All rights reserved.

1. Introduction

The extra low interstitial (ELI) grade of titanium alloy Ti–6Al–4V has been used in the biomedical industry because of its high strength-to-weight ratio, superior mechanical properties over other materials, relatively low elastic modulus, excellent corrosion resistance, and outstanding tissue compatibility [1–4]. Interest in the Ti–6Al–4V ELI alloy for total joint prosthesis grew significantly in the United States toward the late 1970s [4]. Current uses of Ti–6Al–4V alloy include hip and knee joints prosthesis, trauma/fixation devices and dental implants [1].

However, where a contacting motion of counterparts is required, the relatively poor wear resistance of this alloy leads to excessive wear, mechanical and chemical instability, and implant loosening [5]. Various surface treatment methods, such as ion implantation, TiN coating, and thermal oxidation, have thus been proposed to improve the wear resistance by changing the nature of the surface. Thermal oxidation, carried out in normal atmospheric condition containing oxygen and nitrogen, has recently been reported to be a promising approach for producing hard surfaces on Ti alloys [5], where a hardened oxygen diffusion zone (ODZ) formed beneath the TiO₂ layer provided good protection from corrosion and wear [6]. The TiO₂ layer has also found potential applications

in photocatalysis, solar cells, gas sensors and waste remediation [7–9].

With regard to basic characteristics of titanium alloy, such as the equilibrium phase diagram, physical and metallurgical properties, heat treatment process and metallographic structure, there is a lot of useful data for reference. A variety of microstructures can be acquired by simple thermo-mechanical treatments on this $\alpha + \beta$ alloy, with a β transus temperature of about 975 °C [10]. Ti–6Al–4V ELI alloys used in the body implants are inevitably subjected to a variety of loads during walking, running and climbing, which necessitates the knowledge of mechanical properties at different strain rates. Naughton and Tiernan [1] have recently conducted experiments for the strain rate sensitivity index m for the Ti–6Al–4V ELI grade wire alloy at the temperatures ranging from 750 to 1050 °C to determine superplastic forming capabilities. While there are numerous data on the common Ti–6Al–4V alloy, very limited studies involving the strain rate sensitivity and strain hardening characteristics of the ELI grade alloy have been reported. The primary objective of this investigation is, therefore, to evaluate the strain rate sensitivity and the strain hardening exponent of the Ti–6Al–4V ELI alloy subjected to different heat treatment conditions with and without the thermal oxide layer.

2. Experimental procedure

Ti–6Al–4V alloy of ELI grade in an initially annealed condition with a thickness of 3.125 mm was selected in this study. The chem-

* Corresponding author. Tel.: +1 416 979 5000x6487; fax: +1 416 979 5265.
E-mail address: dchen@ryerson.ca (D.L. Chen).

Table 1

Chemical composition of the as-received Ti–6Al–4V ELI alloy selected in the present investigation (wt%).

N	C	H	Fe	O	Al	V	Ti
0.004	0.010	0.0052	0.18	0.10	5.90	4.06	Balance

ical composition of this alloy is given in Table 1. Subsize tensile specimens of 140 mm long with a gauge length of 25 mm and gauge width of 6 mm according to ASTM E8 were machined in the rolling direction using a CNC machine. Heat treatment was carried out at a temperature of 955 °C for 30 min in an argon environment using a Lindberg atmosphere furnace, which was calibrated with chromel–alumel thermocouples in accordance with AMS2750 standard. Two cooling conditions—water quenching and air cooling were used. The specimens were then subjected to aging treatments at a temperature of 525 °C for 4 h in the argon atmosphere at a flow rate of 15 CFH. The as-received and heat-treated specimens were mounted using the bakelite powder, ground with SiC papers of different grades, polished using the 6 μ diamond paste and Master prep solution, and etched with Kroll's reagent (2%HF + 4%HNO₃). The microstructure was observed using a light microscope, and the Knoop hardness values were determined using a computerized Buehler microhardness tester under 200 g.

Post-heat treatment process included cleaning and removing burrs. To reveal the effect of thermal oxide layer on the mechanical properties, some specimens were pickled using HF/HNO₃ solution to remove the oxidized alpha case layer for about 0.2 mm. All samples were hand-ground progressively along the loading direction with 120, 320, and 600 emery papers to achieve a smooth surface. Both pickled and un-pickled specimens oriented in the rolling direc-

tion were subjected to tensile tests using a computerized Instron testing system at a strain rate between 0.01 s^{−1} and 0.00001 s^{−1}. Fracture surfaces after tensile testing were examined using scanning electron microscope (SEM) coupled with energy dispersive X-ray spectroscopy (EDS). Fractal dimensions were determined via three-dimensional (3D) measurements of fracture surfaces areas vs. the ruler scale (i.e., the side length of equilateral triangular tiles) using MeX software. The recorded tensile test data were used to evaluate the strain hardening exponent (or index) n and strain rate sensitivity m in two ways: the common approach [11] and the Lindholm approach [12].

3. Results and discussion

Fig. 1 shows the microstructures of Ti–6Al–4V ELI alloy in different conditions. As seen in Fig. 1(a), the microstructure of the as-received material consisted of primary α and $\alpha + \beta$ phases. Fig. 1(b) shows the microstructure obtained after air cooling from 955 °C and subsequent aging which resulted in a mixture of acicular α and β with primary α , similar to the result obtained by Jovanovic et al. [13] and also described by Donachie [14]. After water quenching from 955 °C and subsequent aging at 525 °C (Fig. 1(c)), the microstructure consisted of primary α and $\alpha' + \beta$. The subsequent aging resulted in precipitation of some fine secondary α phase in the metastable β phase [15]. Semiatin and Bieler [16] confirmed this in their experiments for Ti–6Al–4V alloy and stated that the breakdown operation of microstructure takes place at the two-phase field, below the beta transus temperature at which the β becomes $\alpha + \beta$. The formation of martensite transformed from β phase at 955 °C is due to the fast cooling rate during water quenching, as noted by Zhang et al. [17] for Ti–6Al–4V alloy. They explained

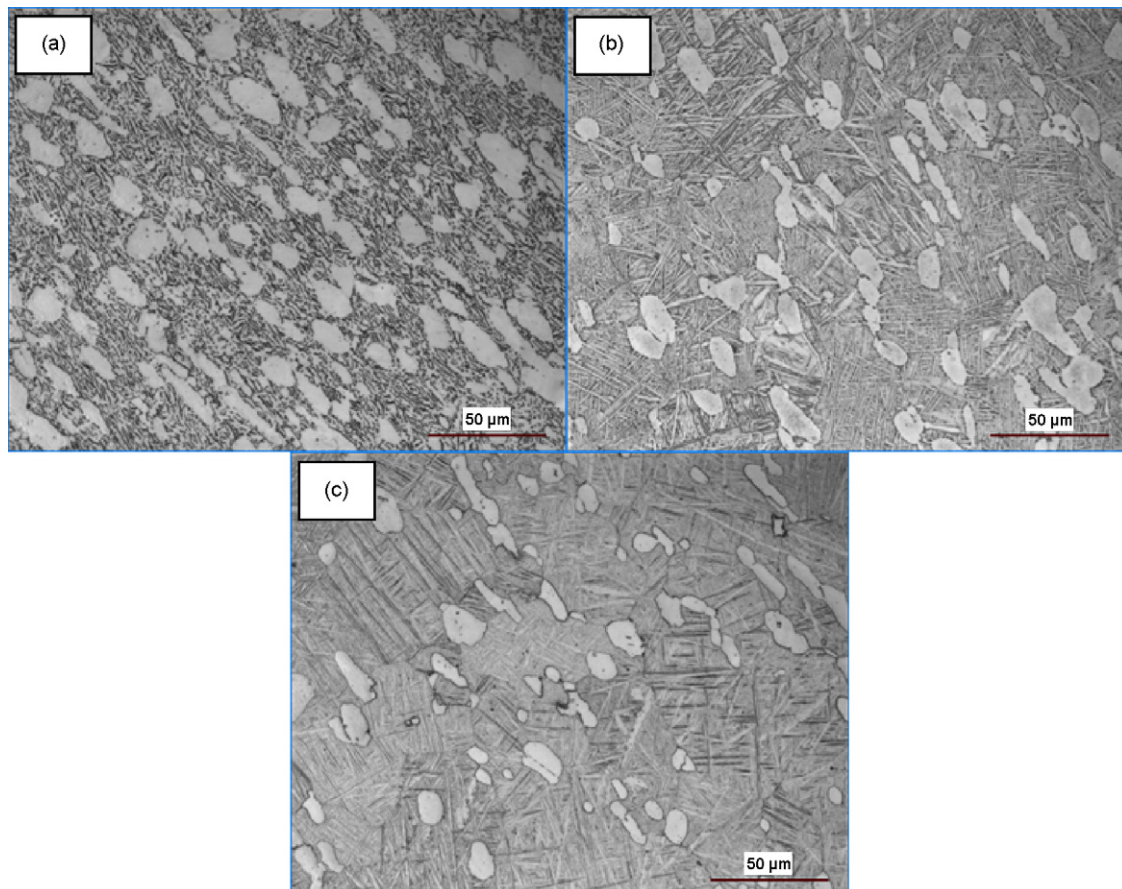


Fig. 1. Microstructures of Ti–6Al–4V ELI alloy in different conditions, (a) as-received, (b) air cooling plus aging (AC + aging), and (c) water quenching plus aging (WQ + aging).

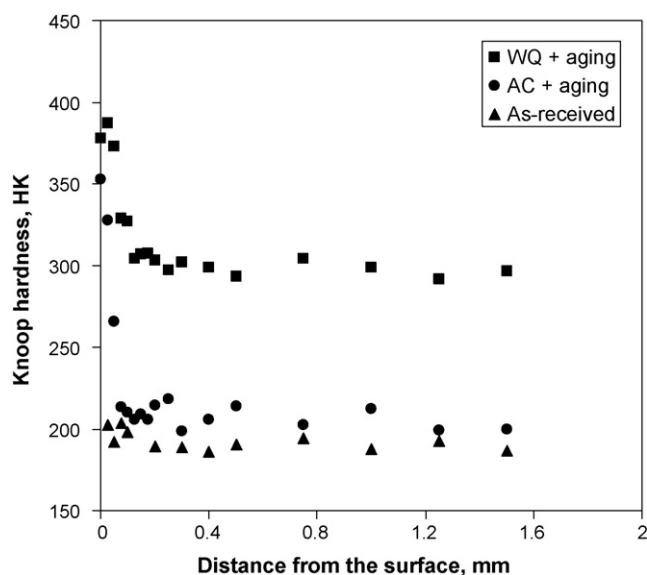


Fig. 2. Knoop microhardness profile of the Ti-6Al-4V ELI alloy in three conditions.

that phase transformation occurs from the high temperature β -Ti to low temperature α -Ti (diffusion controlled when slow cooling) or α' -Ti (shear dominated when rapid cooling). This is in agreement with the microstructure described by Donachie [14]. Jovanovic et al. [13] also reported a similar microstructure after heat treatment at 950 °C followed by water quenching for Ti-6Al-4V alloy.

The obtained microhardness profile is shown in Fig. 2. It is seen that the highest hardness value occurred at the surface of the specimens, indicating that the surface has effectively been hardened. The specimen subjected to water quenching followed by aging (WQ+aging) exhibited much higher hardness values, while the as-received specimen had the lowest hardness out of the three conditions considered in this study. This is in accordance with the results obtained by Jovanovic et al. [13] for Ti-6Al-4V alloy. In general, the hardness increases as the rate of cooling increases. This is due to the formation of martensite arising from rapid cooling [14,17–19]. The hardness of the specimen subjected to air cooling followed by aging (AC+aging) lies in-between those of the WQ+aging and as-received specimens. It can be seen from Fig. 1

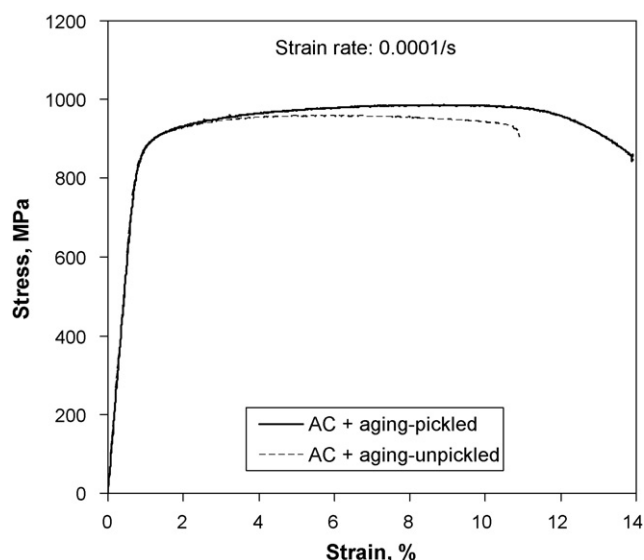


Fig. 3. Stress-strain curves in the AC+aging condition with and without pickling tested at a strain rate of 0.0001 s⁻¹.

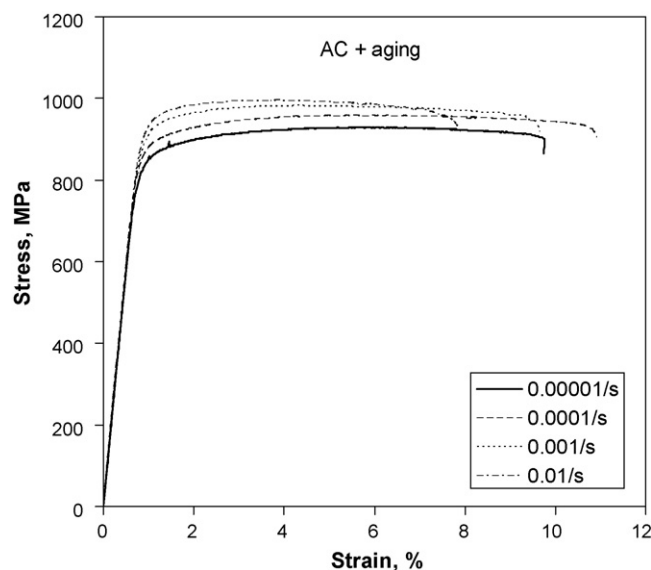


Fig. 4. Effect of strain rates on the stress-strain curves in the AC + aging condition.

that the size of the acicular α is relatively large in the AC + aging condition, when compared to the WQ + aging microstructure which has thin α' plates.

Fig. 3 shows a comparison of the stress-strain curves obtained for the AC + aging specimens with and without pickling tested at a strain rate of 0.0001 s⁻¹. It is seen that the hard oxidized layer of about 0.15 mm had basically no effect on the yield strength and led to only a slight decrease in the ultimate tensile strength (UTS), in spite of some reduction in the ductility. This was in agreement with the results of Ti-6Al-4V alloy reported by Zhu et al. [20] who stated that the oxide scale can induce clefs and degrade the ductility while having little effect on the yield strength and UTS of the alloy. The following results presented will thus be based on the tests of specimens without pickling.

Fig. 4 shows the stress-strain curves for the AC + aging condition tested at different strain rates. As seen from the figure, the curve shifted higher with increasing strain rate, leading to a higher yield strength. Semiatin and Bieler [16] have reported similar results for non-ELI grade of Ti-6Al-4V alloy. The effect of the strain rate on

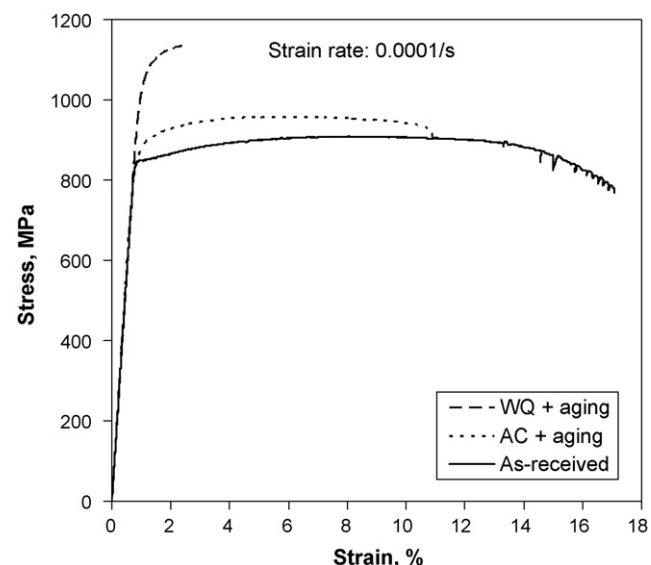


Fig. 5. Stress-strain curves of Ti-6Al-4V ELI alloy in different conditions tested at a strain rate of 0.0001 s⁻¹.

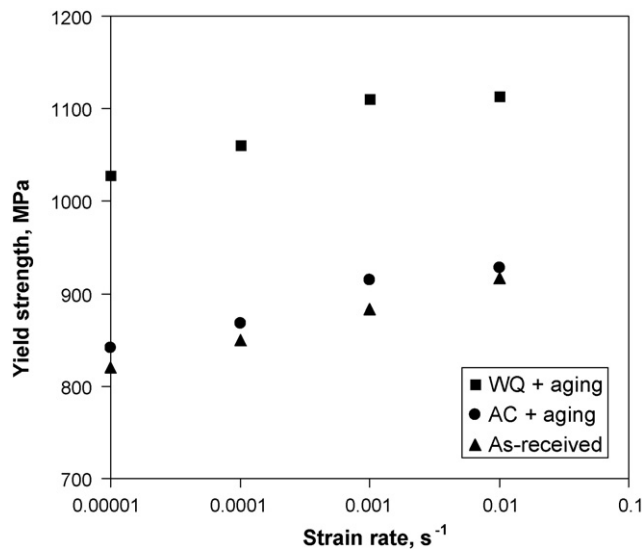


Fig. 6. Yield strength of Ti-6Al-4V ELI alloy in different conditions as a function of strain rates.

the flow stress of Ti-6Al-4V ELI alloy may be described using a power-law [21],

$$\sigma = C\dot{\epsilon}^m, \quad (1)$$

where σ is the flow stress, C is a constant and m is the strain rate sensitivity.

Fig. 5 illustrates the effect of heat treatment conditions on the stress-strain curves at a strain rate of 0.0001 s⁻¹. The WQ + aging condition corresponds to the highest value of the stress but the lowest ductility. This is related to the formation of the martensitic microstructure by the heat treatment.

Fig. 6 shows the variation of yield strength with the strain rate for Ti-6Al-4V ELI alloy in the three conditions. With increasing strain rate the yield strength increases. The WQ + aging heat treatment leads to a much higher yield strength. This trend is also in agreement with the results reported by Semiati and Bieler [16] and Jovanovic et al. [13]. In another study of Ti alloys, Da Rocha et al. [22] presented that the greater strength was associated with rapid cooling in water or oil, where the β phase was transformed into a stronger α' phase

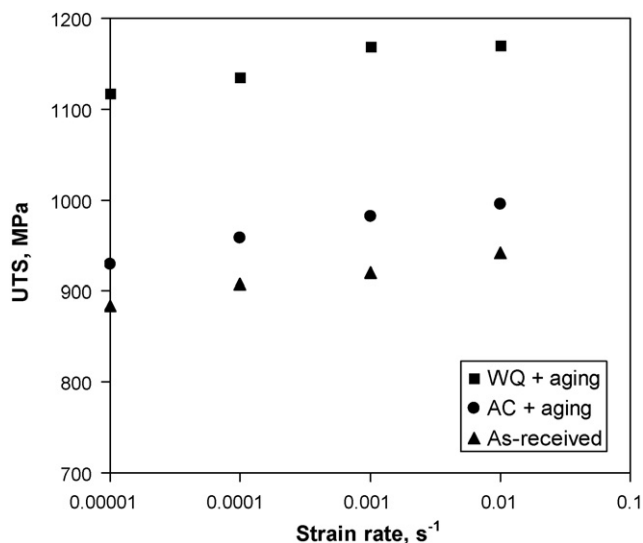


Fig. 7. Ultimate tensile strength (UTS) of Ti-6Al-4V ELI alloy in different conditions as a function of strain rates.

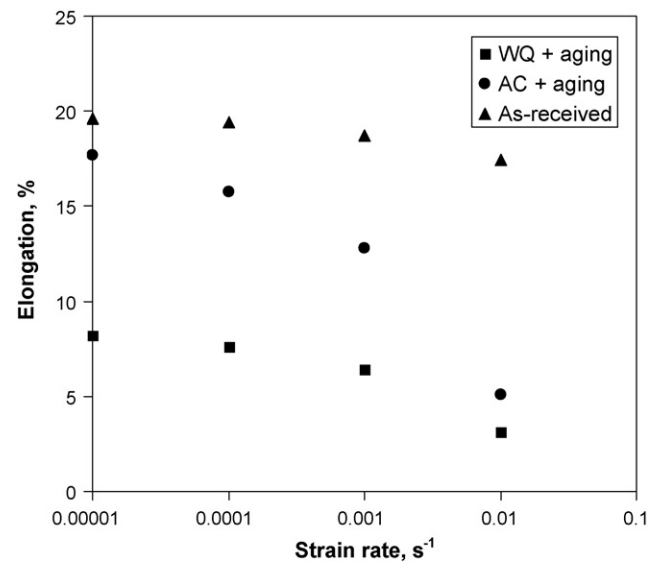


Fig. 8. Elongation of Ti-6Al-4V ELI alloy in different conditions as a function of strain rates.

after quenching in water above 800 °C. The grain size is also related to the velocity at which the material is cooled, and, in general, rapid cooling promotes finer structure.

Fig. 7 shows the ultimate tensile strength (UTS) of this alloy in different conditions as a function of strain rates. Again, the hardest material subjected to WQ + aging corresponds to the highest UTS. This is in accordance with the results by Semiati and Bieler [16], where the peak stress increased with decreasing alpha platelet thickness, and the peak stress was also highest for the martensitic microstructure in Ti-6Al-4V alloy quenched from 955 °C, which were also similar to results obtained by Jovanovic et al. [13]. Fig. 8 shows the effect of strain rate on the ductility for the three material conditions. With increasing strain rate, the ductility decreases. As expected, the hardest material corresponds to the lowest ductility. Similar results were obtained by Jovanovic et al. [13] who stated that the effect of α' and α was the major contributor for these trends. Kwon et al. [23] reported similar results where the highest value of elongation corresponds to a discontinuity of the α

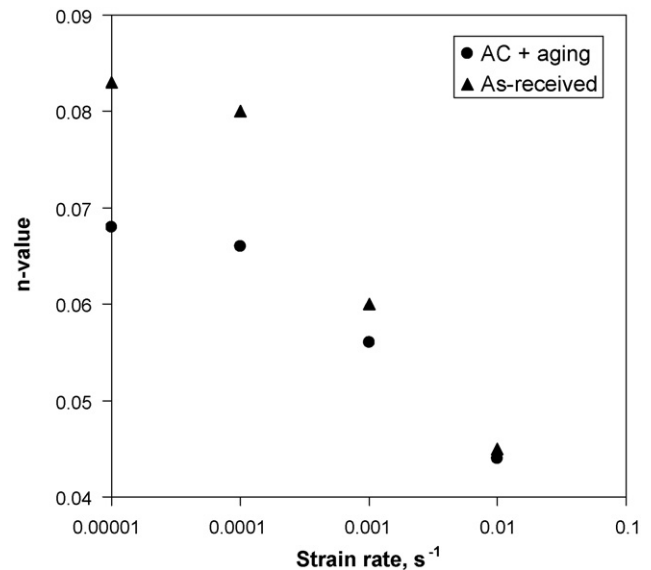


Fig. 9. Variation of strain hardening exponent n evaluated on the basis of Holloman equation with the strain rate in the as-received and AC + aging conditions.

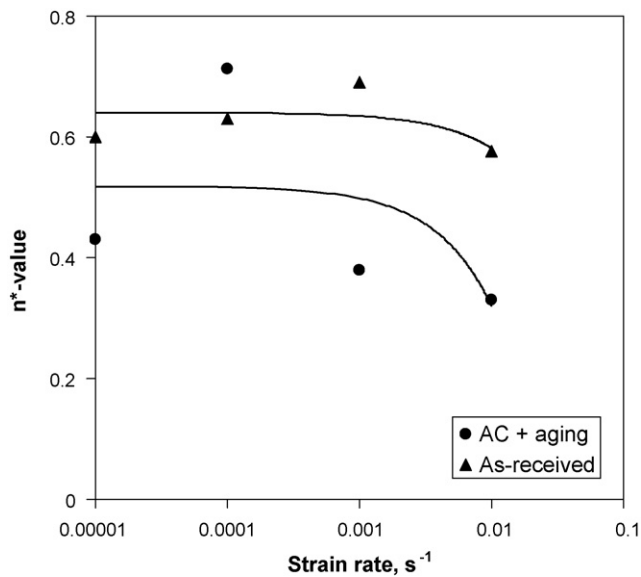


Fig. 10. Strain hardening exponent n^* as a function of strain rates in the as-received and AC + aging conditions.

phase (in which slip can easily occur) because of the impediment of the β phase. The more drastic decrease in ductility or a stronger dependence of ductility on the strain rate in the AC + aging condition, compared to other conditions, is associated with the bigger difference of microhardness values between the hardened surface layer and interior (Fig. 2), where the surface hardness in both heat treatment conditions is nearly the same but the AC + aging condition has a much lower internal hardness which is directly related to the microstructure shown in Fig. 1(b). Such a big hardness difference between the surface and interior would cause deformation mismatch or incompatibility, resulting in a lower ductility at higher strain rates.

Fig. 9 shows the variation of strain hardening exponent with the strain rate for the as-received and AC + aging conditions. It should

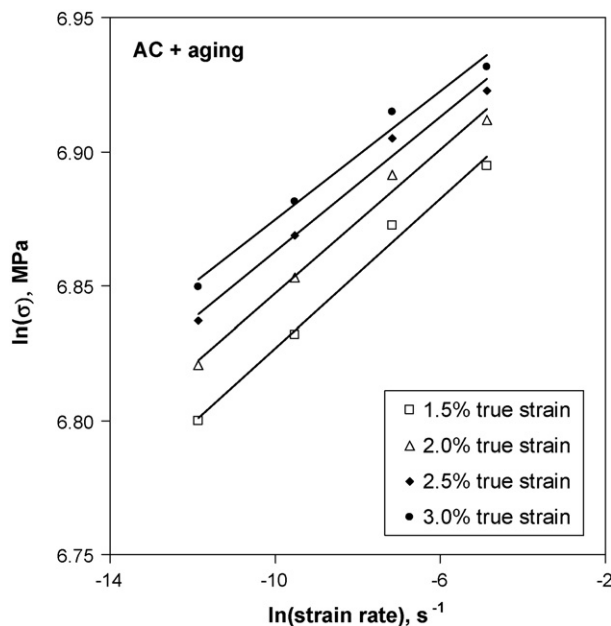


Fig. 11. A typical plot of $\ln(\text{stress})$ vs. $\ln(\text{strain rate})$ to evaluate the strain rate sensitivity, m , at different true strain values via the common approach for the AC + aging specimens.

Table 2

Strain rate sensitivity values for the air cooling plus aging (AC + aging) specimens, evaluated via the common approach (m) and Lindholm approach (m_L).

True strain, %	m	m_L
1.5	0.0139	30.22
2.0	0.0134	29.58
2.5	0.0126	28.14
3.0	0.0120	27.11

be noted that no strain hardening exponent in the WQ + aging condition is considered due to the low ductility or very short regime of plastic deformation (Fig. 5). In Fig. 9 the value of n is evaluated using the following Holloman relationship,

$$\sigma = K\epsilon^n, \quad (2)$$

suggested in ASTM E646 to describe approximately the flow curve in the uniform deformation stage, where K is the strength coefficient and n is the strain hardening exponent. It is seen that the n values decreased with increasing strain rate. This was also reported to be the case by Jain et al. [24] and El-Domiatiy [25] for Ti–6Al–4V alloy. Tang et al. [26] reported similar results for metallic materials and proposed the following relationship between strain hardening exponent (n) and the strain rate ($\dot{\epsilon}$),

$$n = n_0 - b \lg \dot{\epsilon}, \quad (3)$$

where n_0 is a material constant, and b is the slope in the n vs. $\lg \dot{\epsilon}$ graph. As the strain rate increased, the strain hardening exponent decreased proportionally. The value of n is seen to be higher for the as-received condition than for the AC + aging condition at all the strain rates.

Fig. 10 shows the effect of the strain rate on the strain hardening exponent evaluated on the basis of a modified relationship proposed by Afrin et al. [27],

$$\sigma - \sigma_y = K(\epsilon - \epsilon_y)^{n^*}, \quad (4)$$

where σ_y is the yield strength, ϵ_y is the yield strain, K is a constant and n^* is the strain hardening exponent. In Eq. (4) the elastic

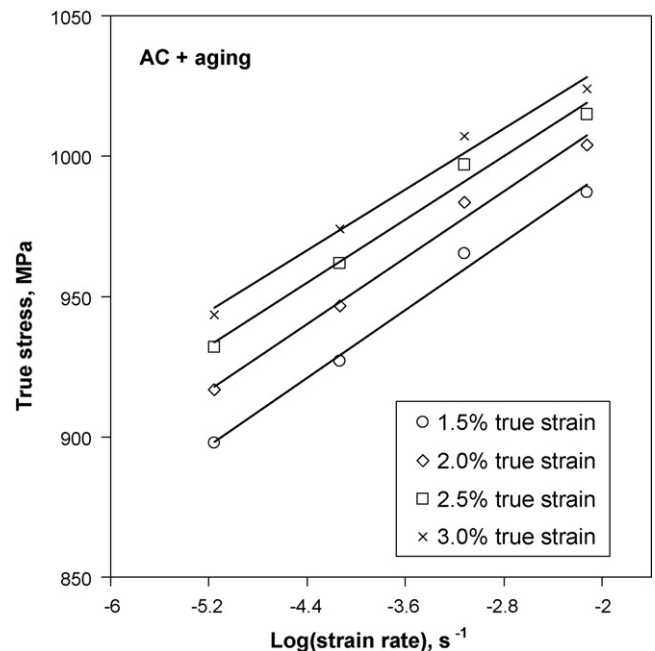


Fig. 12. A typical plot of true stress vs. $\log(\text{strain rate})$ to determine the strain rate sensitivity, m_L , at different true strain values via the Lindholm approach for the AC + aging specimens.

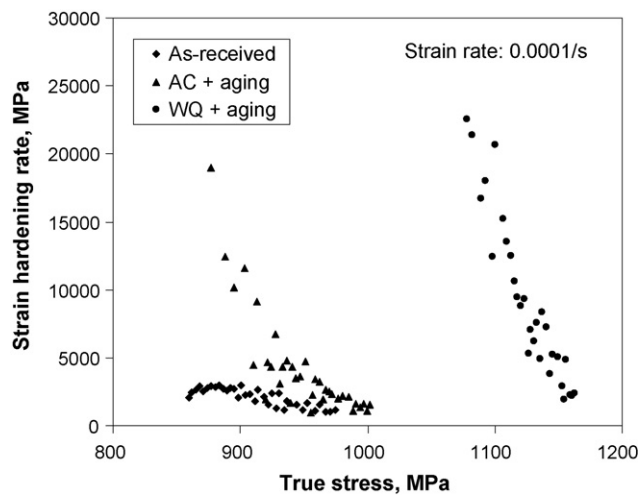


Fig. 13. Strain hardening rate as a function of true stress for the Ti-6Al-4V ELI alloy in three conditions tested at a strain rate of 0.0001 s^{-1} .

component in both stress and strain is indeed eliminated. While the n^* values do not seem to be so sensitive to the strain rate, the as-received condition also exhibits a higher strain hardening exponent, compared to the AC + aging condition. Besides, the n^* values evaluated on the basis of Eq. (4) are much larger than the n values evaluated based on Eq. (2).

Fig. 11 shows the curves of $\ln(\sigma)$ vs. $\ln(\text{strain rate})$ at different true strain values in the AC + aging condition, where the slope indicates the strain rate sensitivity, m , in the common approach [8,18]. The obtained strain rate sensitivity is shown in Table 2. It is seen

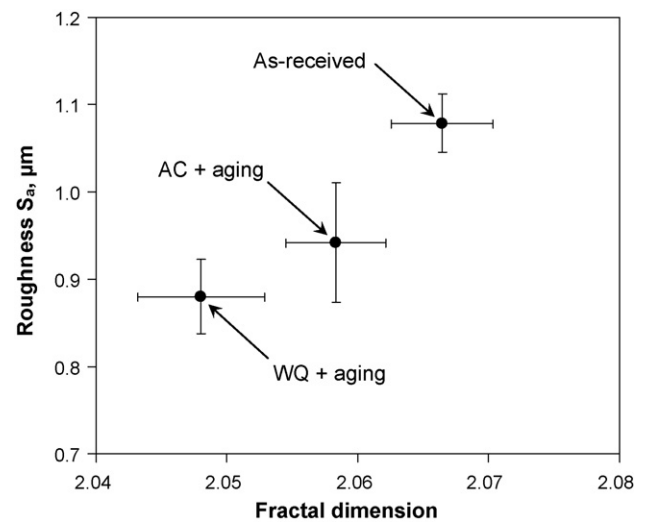


Fig. 14. Relationship between the roughness, S_a , and fractal dimension of fracture surfaces of the Ti-6Al-4V ELI alloy in the three conditions, via three-dimensional (3D) measurements on the fracture surfaces.

that the strain rate sensitivity decreases with increasing true strain. Similar results have also been reported by Lin and Chen [28]. The Lindholm approach [12] is further used to evaluate the strain rate sensitivity based on the following equation,

$$\sigma = \sigma_{10}(\epsilon) + \sigma_1(\epsilon) \log \dot{\epsilon} \quad (5)$$

The Lindholm strain rate sensitivity, m_L , is the slope, $\sigma_1(\epsilon)$, of σ vs. $\log \dot{\epsilon}$ based on the above equation. A typical plot of σ vs. $\log \dot{\epsilon}$ at

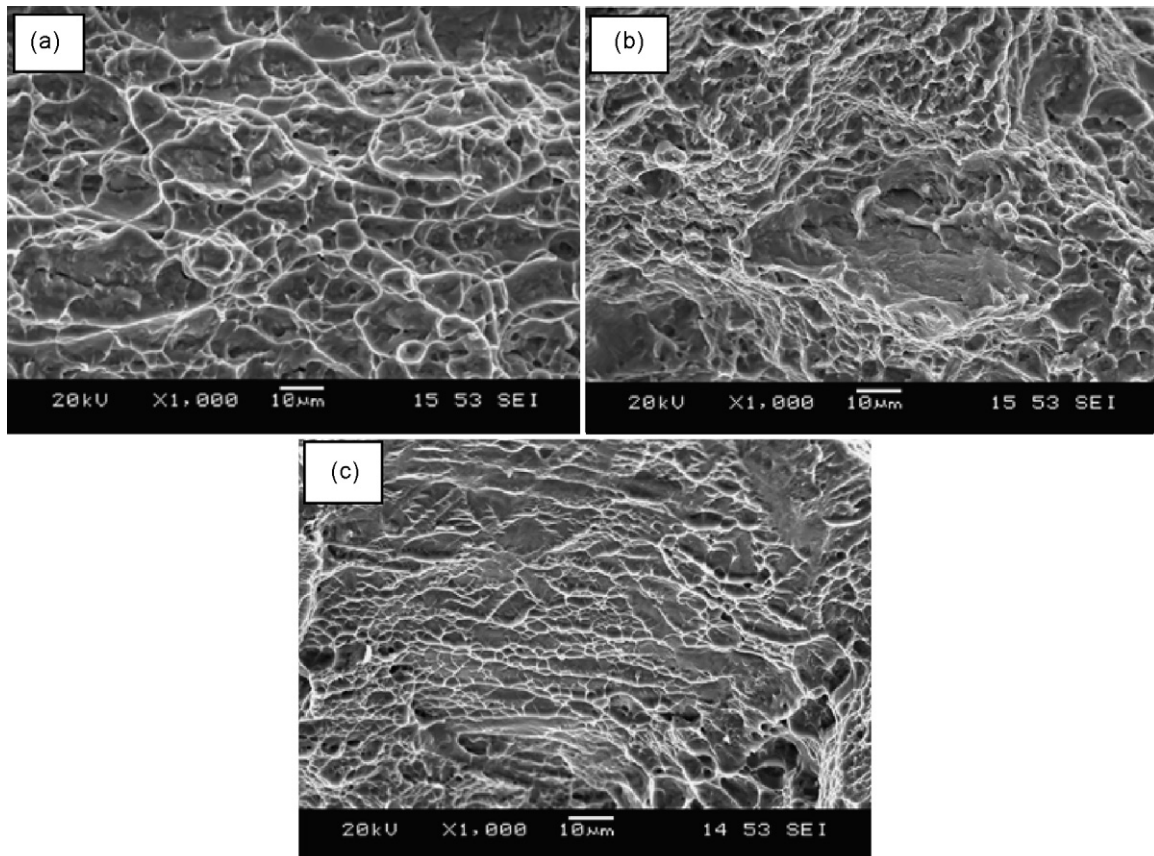


Fig. 15. SEM micrographs of fracture surfaces of the Ti-6Al-4V ELI alloy in three conditions tested at a strain rate of 0.0001 s^{-1} , (a) as-received, (b) AC + aging, and (c) WQ + aging.

different true strain values is shown in Fig. 12, and the evaluated m_L [or $\sigma_1(\epsilon)$] is also given in Table 2. Again, the strain rate sensitivity decreases as the true strain increases. The Lindholm strain rate sensitivity values are much larger than the strain rate sensitivity values evaluated via the common approach. However, both the common and Lindholm strain rate sensitivity values decrease monotonically with increasing true strain. Similar results were also reported in non-ELI grade of Ti–6Al–4V [24], extruded AZ31 magnesium alloy [28] and ultrafine-crystalline Cu [29].

Fig. 13 shows the work hardening rate as a function of true stress for the Ti–6Al–4V ELI alloy in the three conditions tested at a strain rate of 0.0001 s^{-1} . It is seen that there is a higher initial work hardening rate for the WQ + aging material, because of higher dislocation densities generated as observed by Markandeya et al. for Cu–Ti–Cd alloy [30]. Kruger et al. [15] also reported that water quenching led to higher hardness values due to a much higher dislocation density and sometimes twins in Ti–6Al–4V alloy. A similar phenomenon was observed by Praveen et al. [31] for Ni-based superalloy IN718.

Fig. 14 shows a relationship between the three-dimensional (3D) fractal dimension and roughness of fracture surfaces of the Ti–6Al–4V ELI alloy in different conditions tested at a strain rate of 0.0001 s^{-1} . Fractal dimension is found to be the highest in the as-received condition, which is related to the highest ductility as shown in Fig. 8, and the lowest in the WQ + aging condition due to the lowest ductility, with the AC + aging condition lying in-between the two conditions. It is also seen that the fractal dimension increases as the roughness increases. That is, the rougher the fracture surface, the higher the fractal dimension. This is in good agreement with the results reported in the literature [32–35]. The morphology and roughness of fracture surfaces are shown in Fig. 15. The as-received material exhibited a characteristic dimple-like ductile fracture with a large number of tear ridges, as seen from Fig. 15(a). The fracture surface of the AC + aging, Fig. 15(b), consisted of dimples with some cleavage-like facets, and the surface roughness was visibly less when compared to the as-received specimen (Fig. 15(a)). In the WQ + aging specimen, Fig. 15(c), the fracture mode exhibited more of cleavage cracking in conjunction with some dimples, thus resulting in a lower surface roughness compared to the as-received and AC + aging cases. This is attributed to the presence of martensite arising from the water quenching as discussed in the earlier part of this section.

4. Conclusions

1. The as-received Ti–6Al–4V ELI alloy consisted of primary α and $\alpha + \beta$ phases. After air cooling and aging (AC + aging), the microstructure became a mixture of acicular α and β with primary α . After water quenching and aging (WQ + aging), the microstructure consisted of primary α and $\alpha' + \beta$ plus some fine secondary α phase in the β phase.
2. Both WQ + aging and AC + aging heat treatment procedures led to an effective surface hardening arising from the formation of an oxidized layer of about 0.15 mm in depth. While the AC + aging moderately increased the interior hardness, the WQ + aging significantly increased the internal hardness by about 50% due to the formation of martensite. The formed surface layer seemed to have no effect on the yield strength (YS) and only have a slight decrease in the ultimate tensile strength (UTS), although a certain reduction in the ductility was observed.
3. The YS and UTS were the highest for the WQ + aging specimen and the lowest for the as-received specimen. On the contrary, the ductility was the highest in the as-received condition and the lowest in the WQ + aging condition. Both strength and ductility in the AC + aging condition lay in-between those in other two conditions. As the strain rate increased, both YS and UTS increased and the ductility decreased.

4. The strain hardening exponent was observed to decrease with increasing strain rate, and the softer as-received material exhibited a higher strain hardening exponent. The modified evaluation gave a higher strain hardening exponent. The harder materials showed a higher initial work hardening rate due to a higher dislocation density and sometimes twins. The strain rate sensitivity was found to decrease with increasing true strain. The Lindholm strain rate sensitivity values were much larger than those evaluated using the common approach.
5. Fractal dimension was observed to be the highest in the as-received condition, corresponding to the highest ductility, and the lowest in the WQ + aging condition due to the lowest ductility. The fractal dimension increased as the roughness of fracture surfaces increased.
6. The as-received material exhibited a characteristic dimple-like ductile fracture with a large number of tear ridges. The fracture surface of the AC + aging specimen consisted of dimples with some cleavage-like facets. The fracture mode in the WQ + aging condition exhibited more of cleavage cracking in conjunction with some dimples.

Acknowledgements

The authors would like to thank the Natural Sciences and Engineering Research Council of Canada (NSERC) for providing financial support. One of the authors (DLC) is also grateful for the financial support by the Premier's Research Excellence Award (PREA), Canada Foundation for Innovation (CFI) and Ryerson Research Chair (RRC) programs. The authors would also like to thank Q. Li, A. Machin, J. Amankrah, D. Ostrom and R. Churaman for their assistance in the experiments.

References

- [1] M.D. Naughton, P. Tiernan, *Proc. Inst. Mech. Eng., Part L, J. Mater.: Des. Appl.* 221 (2007) 165–174.
- [2] R.T. Bothe, L.E. Beaton, H.A. Davenport, *Surg. Gynecol. Obstet.* 71 (1940) 598–602.
- [3] G.S. Leventhal, *J. Bone Joint Surg.* 33-A (2) (1951) 473–474.
- [4] K. Wang, *Mater. Sci. Eng. A* 213 (1996) 134–137.
- [5] H. Guleryuz, H. Cimenoglu, *Surf. Coat. Technol.* 192 (2005) 164–170.
- [6] P.A. Dearnley, K.L. Dahm, H. Cimenoglu, *Wear* 256 (2004) 469–479.
- [7] S. Wendt, P.T. Sprunger, E. Lira, G.K.H. Madsen, Z. Li, J.O. Hansen, J. Matthiesen, A.B. Rasmussen, E. Laegsgaard, B. Hammer, F. Besenbacher, *Science* 320 (2008) 1755–1759.
- [8] N. Shibata, A. Goto, S.Y. Choi, T. Mizoguchi, S.D. Findlay, T. Yamamoto, Y. Ikuhara, *Science* 322 (2008) 570–573.
- [9] R. Schoelgl, *Nat. Mater.* 7 (2008) 772–774.
- [10] T. Seshacharyulu, S.C. Medeiros, J.T. Morgan, J.C. Malas, W.G. Frazier, Y.V.R.K. Prasad, *Mater. Sci. Eng. A* 279 (2000) 289–299.
- [11] G.E. Dieter, *Mechanical Metallurgy*, 3rd Ed., McGraw-Hill, 1986.
- [12] U.S. Lindholm, *J. Mech. Phys. Solids* 12 (1964) 317–335.
- [13] M.T. Jovanovic, S. Tadic, S. Zec, Z. Miskovic, I. Bobic, *Mater. Des.* 27 (2006) 192–199.
- [14] M.J. Donachie Jr., *Titanium—A Technical Guide*, 2nd Ed., ASM International, 2000.
- [15] L. Kruger, K. Sommer, T. Halle, M. Hockauf, L.W. Meyer, *J. Phys. IV* 134 (2006) 1091–1096.
- [16] S.L. Semiatin, T.R. Bieler, *Acta Mater.* 49 (2001) 3565–3573.
- [17] W. Zhang, B. Wu, W.S. Zhao, D.X. Li, M.L. Sui, *Mater. Sci. Eng. A* 438–440 (2006) 320–323.
- [18] H. Fujii, H.G. Suzuki, *J. Iron Steel Inst. Jpn.* 77 (1991) 1481–1488.
- [19] W.D. Callister Jr., *Materials Science and Engineering—An Introduction*, 7th Ed., John Wiley & Sons, Inc., 2007.
- [20] X.J. Zhu, M.J. Tan, S. Thiruvardhelvan, *Mater. Sci. Forum* 29 (2005) 233–237.
- [21] W.F. Hosford, *Mechanical Behavior of Materials*, 4th Ed., Cambridge University Press, 1999.
- [22] S.S. Da Rocha, G.L. Adabo, L. Geraldo Vaz, G.E.P. Henriques, *J. Mater. Sci.: Mater. Med.* 16 (2005) 759–766.
- [23] J.D. Kwon, Y.T. Bae, S.J. Choi, *Int. J. Mod. Phys. B* 17 (2003) 1297–1303.
- [24] M. Jain, M.C. Chaturvedi, N.L. Richards, N.C. Goel, *Mater. Sci. Eng. A* 138 (1991) 205–211.
- [25] A. El-Domiaty, *J. Mater. Proc. Technol.* 32 (1992) 243–251.
- [26] C. Tang, J. Zhu, Y. Zhang, H. Zhou, *Acta Metall. Sin.* (English Edition), Series B: Process Metall. Miscellaneous 7 (1994) 183–186.

- [27] N. Afrin, D.L. Chen, X. Cao, M. Jahazi, Scripta Mater. 57 (2007) 1004–1007.
- [28] X.Z. Lin, D.L. Chen, J. Mater. Eng. Perform. 17 (2008) 894–901.
- [29] Y.F. Shen, L. Lu, M. Dao, S. Suresh, Scripta Mater. 55 (2006) 319–322.
- [30] R. Markhandeya, S. Nagarjuna, D.V.V. Satyanarayana, Mater. Sci. Eng. A 248 (2006) 233–243.
- [31] K.V.U. Praveen, G.V.S. Sastry, V. Singh, Metall. Mater. Trans. A 39 (2008) 65–78.
- [32] B.B. Manderbrot, D.E. Passoja, A.J. Paullay, Nature 308 (1984) 721–722.
- [33] O.A. Hilders, L. Sáenz, M. Ramos, N.D. Pena, JMEPEG 8 (1999) 87–90.
- [34] O.A. Hilders, M. Ramos, N.D. Pena, L. Saenz, J. Mater. Sci. 41 (2006) 5739–5742.
- [35] B. Venkatesh, D.L. Chen, S.D. Bhole, Scripta Mater. 59 (2008) 391–394.